The Seismic Record
A journal of the Seismological Society of America

A Spectrum of Elastic and Inelastic Distributed Surface Deformation: Remote Observations of the 2026 Venezuela Earthquakes

OPEN ACCESS

Catherine Hanagan*[1], Nadine Reitman[2], Omar Pérez[3], Harriet Yin[2], Stephen DeLong[1], Johanna Nevitt[1], Chris DuRoss[2], Alexandra Hatem[2], Jessica Thompson Jobe[2], Sylvia Nicovich[2], and Joseph Powell[2]

Abstract

On 24 June 2026, moment magnitude (M_w) 7.2 and 7.5 earthquakes struck northern Venezuela along the right-lateral Boconó and San Sebastián faults, initiating on land west of Morón. Intense shaking and damage, with preliminary subsurface slip estimates, indicate >215 km long, ~70% offshore eastward rupture propagation, complicating understanding of the shallow rupture process. We investigate surface deformation near five coastal towns intersecting the fault through mapping and subpixel correlation of high-resolution (0.4–10 m) optical imagery. Near Morón, ~0.78 m of fault-parallel displacement is distributed over >3 km without surface rupture. To the east, displacements increase within narrower zones along towns built on alluvium, from an average of 2.7 m within 69 m at Caraballeda tapering to an average of 0.3 m within 340 m at Camurí Grande. Despite >3 m displacement at Caraballeda, <300 m long discontinuous surface rupture was identified. Airport runway cracking between June 25 and 26 coincides with 0.1–0.2 m of secondary fault afterslip. Shear strains support primarily elastic surface deformation in the west above a fault slip deficit and permanent inelastic deformation consistent with plastic yielding above shallow fault slip in the east. These observations highlight the importance of characterizing distributed near-surface strain and material properties for understanding fault displacement hazard.

Cite this article as Hanagan, C., N. Reitman, O. Pérez, H. Yin, S. DeLong, J. Nevitt, C. DuRoss, A. Hatem, J. Thompson Jobe, S. Nicovich, and et al. (2026). A Spectrum of Elastic and Inelastic Distributed Surface Deformation: Remote Observations of the 2026 Venezuela Earthquakes, *The Seismic Record*. **6**(**4**), 400–410, doi: 10.1785/0320260037.

Supplemental Material

Introduction

At 06:04 p.m. local time on 24 June 2026 in northern Venezuela, a moment magnitude (M_w) 7.2 earthquake was followed by an M_w 7.5 earthquake <40 s later. The earthquakes devastated coastal communities with estimated fatalities in the tens of thousands and economic losses in the billions (USD; see Data and Resources). "Did You Feel It?" reports indicate the most intense shaking occurred east of the M_w 7.2 epicentral region, causing closure of the Simón Bolívar International Airport east of Catia La Mar, and widespread damage and coastal building collapse as far as Camurí Grande, ~190 km east of the initial epicenter (see Data and Resources; Martinez, 2026; Fig. 1). The sequence initiated onshore southeast of Yumare and offshore west of Catia La Mar at depths of ~10 km on the dextral Boconó–San Sebastián–El Pilar fault system that separates the South American plate from the Caribbean plate with a relative motion of ~20 mm/yr

1. U.S. Geological Survey, Earthquake Science Center, Moffett Field, California, U.S.A., https://orcid.org/0000-0002-2966-5175 (CH); https://orcid.org/0000-0002-0945-2172 (SDL); https://orcid.org/0000-0003-3819-1773 (JN); 2. U.S. Geological Survey, Geologic Hazards Science Center, Golden, Colorado, U.S.A., https://orcid.org/0000-0002-6730-2682 (NR); https://orcid.org/0000-0002-0670-6579 (HY); https://orcid.org/0000-0002-6963-7451 (CDR); https://orcid.org/0000-0001-7584-2235 (AH); https://orcid.org/0000-0001-5574-4523 (JTJ); https://orcid.org/0000-0003-4280-4034 (SN); https://orcid.org/0009-0004-8272-1043 (JP); 3. Simón Bolívar University, Caracas, Venezuela

*Corresponding author: chanagan@usgs.gov

© 2026. The Authors. This is an open access article distributed under the terms of the CC-BY license, which permits unrestricted use, distribution, and reproduction in any medium, provided the original work is properly cited.

Downloaded from pubs.geoscienceworld.org/ssa/tsr/article-pdf/6/4/400/8403143/tsr-2026037.1.pdf by guest on 21 October 2026

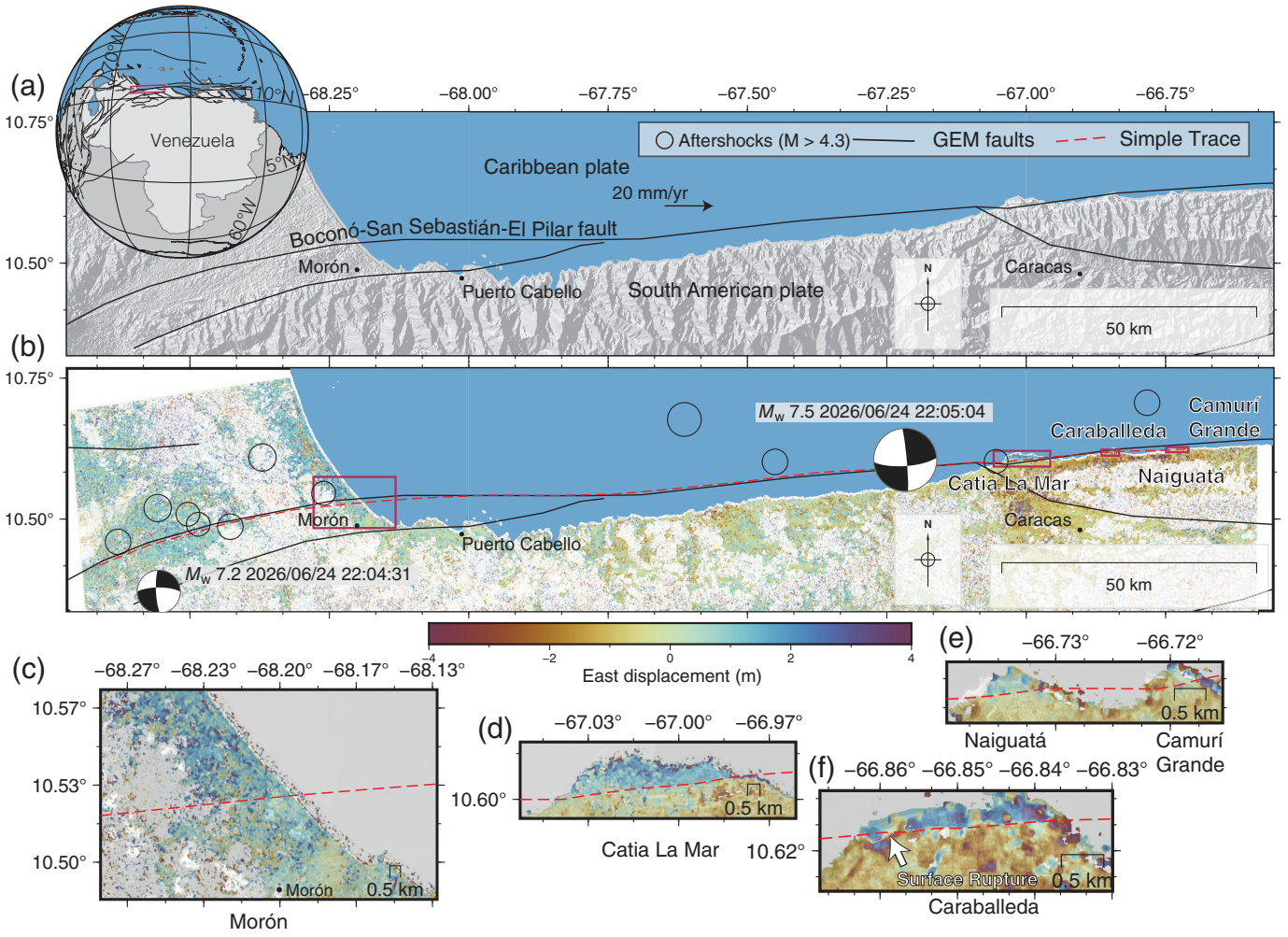


Figure 1. Overview of the tectonic setting and deformation associated with the 2026 M_w 7.2 and 7.5 Venezuela earthquakes. (a) Major faults (black lines from Global Earthquake Model [GEM]; Styron and Pagani, 2020) overlain on shaded relief from the Shuttle Radar Topography Mission (Farr *et al.*, 2007). The earthquakes occurred on the Boconó and San Sebastián faults, which separate the South American plate from the Caribbean plate to the north, with a relative motion of ~20 mm/yr due east (Weber *et al.*, 2001). (b) East–west displacement from Sentinel-2 optical image subpixel correlation with the simple inferred fault trace (red dashed line) for both earthquakes and event epicenters marked by their moment tensor solutions from the U.S. Geological Survey (USGS) (see Data and Resources). Aftershocks with magnitude (M) > 4.3 are plotted as black rings scaled by magnitude. (c–f) High-resolution (10 m) east–west displacement maps from Sentinel-2 for each fault-crossing town along the coast. The white arrow on Caraballeda (f) marks the location of surface rupture noted in the field and shown in Figure 3.

(Fig. 1; Audemard *et al.*, 2000; Pérez *et al.*, 2001; Weber *et al.*, 2001). Initial subsurface slip estimates from the U.S. Geological Survey (USGS) finite-fault model depict eastward rupture propagation over 215 km with maximum slip of 1.8 m at seismogenic depths (>8 km). East of the epicenters near Morón, the Boconó fault merges with the San Sebastián fault and continues offshore. The fault then extends onshore across alluvial fans sourced from the Cordillera de la Costa (Venezuelan Coastal Range) at the four coastal towns of Catia La Mar, Caraballeda, Naiguatá, and Camurí Grande (Fig. 1; Audemard *et al.*, 2000; Larsen *et al.*, 2002). Approximately 70% of the total rupture occurred offshore, hindering rapid, direct measurements of surface rupture.

Scaling relationships for an M_w 7.56 strike-slip earthquake, the combined magnitude of these earthquakes, predicts 1–3 m of average slip along a surface rupture proportional to ~80% of the length at depth (>170 km; Wells and Coppersmith, 1994; Thingbaijam *et al.*, 2017). Therefore, significant surface rupture is expected from prior observed ruptures, and historical earthquakes without extensive discrete surface rupture tend to have lower magnitudes (e.g., M_w 6.6 Bam, Iran, Fialko *et al.*, 2005; M_w 6.0 Napa, California, Nevitt *et al.*, 2020). The

Downloaded from pubs.geoscienceworld.org/ssa/tsr/article-pdf/6/4/400/8403143/tsr-2026037.1.pdf by guest on 21 October 2026

magnitude of the 2026 Venezuela earthquakes and initial modeled slip estimates would predict clear surface rupture along the fault from the USGS finite fault model (see Data and Resources). Absence of surface rupture would raise concern for remaining shallow elastic strain that could drive further fault slip. The ~30% onshore portion of the earthquakes offers a glimpse of the shallow rupture process. The absence of surface rupture would raise concern for remaining shallow elastic strain that could drive further fault slip.

Shallow slip deficits are commonly inferred for strike-slip earthquakes, where slip at the surface is less than the modeled slip at depth (e.g., Fialko *et al.*, 2005; Kaneko and Fialko, 2011; Antoine *et al.*, 2024). A shallow slip deficit may be accompanied by elastic surface deformation as well as potentially permanent inelastic deformation, each with different implications for seismic hazard. If deformation is primarily elastic, the inferred shallow slip deficit may coincide with a portion of the fault with less strain accumulation due to prior slip; or, it may represent residual elastic strain available to drive subsequent afterslip, interseismic creep, and/or earthquake slip (e.g., Marone *et al.*, 1991; Fialko *et al.*, 2005; Brooks *et al.*, 2017). Alternatively, a deficit may also be associated with inelastic distributed deformation, which accommodates permanent strain across a finite zone rather than along a single throughgoing rupture plane (e.g., Antoine *et al.*, 2024). Inelastic strain can pose an immediate hazard to surficial or buried infrastructure and encapsulates several processes, such as fracturing, granular flow, and folding (e.g., Rodriguez Padilla *et al.*, 2022). These processes operate over a variety of length scales, from immediately adjacent to the fault, as shown in paleoseismic trenches (e.g., Brooks *et al.*, 2017), to kilometers away from the fault, as noted by widespread earthquake damage zones (e.g., Rodriguez Padilla *et al.*, 2022; Antoine *et al.*, 2024). Ultimately, distributed deformation may reflect a spectrum of both elastic and inelastic processes that are not uniquely resolvable with geodetic data alone because both modes produce indistinguishable patterns of surface deformation (e.g., from elastic and elastoplastic models; Nevitt *et al.*, 2020). However, understanding the contributions of elastic and inelastic strain to observed distributed deformation can provide insight for immediate and future fault hazard.

Remote observations over the coastal towns provide a first look at characterizing and understanding near-fault surface deformation from the Venezuela earthquakes, including the possible contributions of elastic and inelastic deformation. Toward this end, we use high-resolution (0.4–10 m) satellite optical imagery to map potential surface rupture, identify and measure offset features, and derive 2D horizontal displacement fields via subpixel correlation.

Methods

Our analysis focuses on five key locations: Morón near the M_w 7.2 epicentral region to the west, and Catia La Mar, Caraballeda, Naiguatá, and Camurí Grande to the east along the northern coast (Fig. 1). We use pre- and post-earthquake imagery to map surface rupture and offset features, derive surface displacement fields, and calculate fault-parallel displacements (or offsets) and deformation zone widths, as described in the associated data release (Hanagan, Reitman, *et al.*, 2026). Surface displacement fields are calculated via subpixel correlation of Sentinel-2 optical imagery for Morón (10 m resolution), and WorldView optical imagery for each of the other coastal towns (0.4 m resolution; table S1 of Hanagan, Reitman, *et al.*, 2026). We process one time span of images at each location except for Catia La Mar, where a partly cloudy image acquired on June 25 permits analysis of potential afterslip at the Simón Bolívar International Airport with a second image on June 26. We derive a simple inferred fault trace from the optical displacement fields, Sentinel-1 Interferometric Synthetic Aperture Radar (InSAR), and pre-existing fault mapping (Audemard *et al.*, 2000) and topography at ~1:50:000 scale. Fault-parallel displacements and deformation zone widths are calculated from two-sloped error function fits to fault-perpendicular displacement swaths sampled every 100 m along the simple fault (Figs. 2 and 3, and Methods and fig. S1 of Hanagan, Reitman, *et al.*, 2026; Milliner *et al.*, 2021). Swaths are 2000-m-long by 50-m-wide for the coastal towns and 15000-m-long by 500-m-wide at Morón (Fig. S1 of Hanagan, Reitman, *et al.*, 2026). We report fault-parallel displacement uncertainties as the standard deviation of the residuals to the error function fit, and deformation zone widths that capture 95% (2-standard deviations) of the total fault-parallel displacement. The deformation zone width is likely a maximum estimate, due to the inherent smoothing of the subpixel correlation. The deformation zone width 1-standard deviation uncertainty is derived from the covariance of the error function parameter fit, and tends to underestimate the actual uncertainty by visual inspection. For later discussion, we also calculate the peak fault-parallel shear strain from the error function fit derivatives, neglecting the small far-field slope terms (see Milliner *et al.*, 2021, their equation 2; Hanagan, Reitman, *et al.*, 2026). Strains from the error function

Downloaded from pubs.geoscienceworld.org/ssa/tsr/article-pdf/6/4/400/8403143/tsr-2026037.1.pdf by guest on 21 October 2026

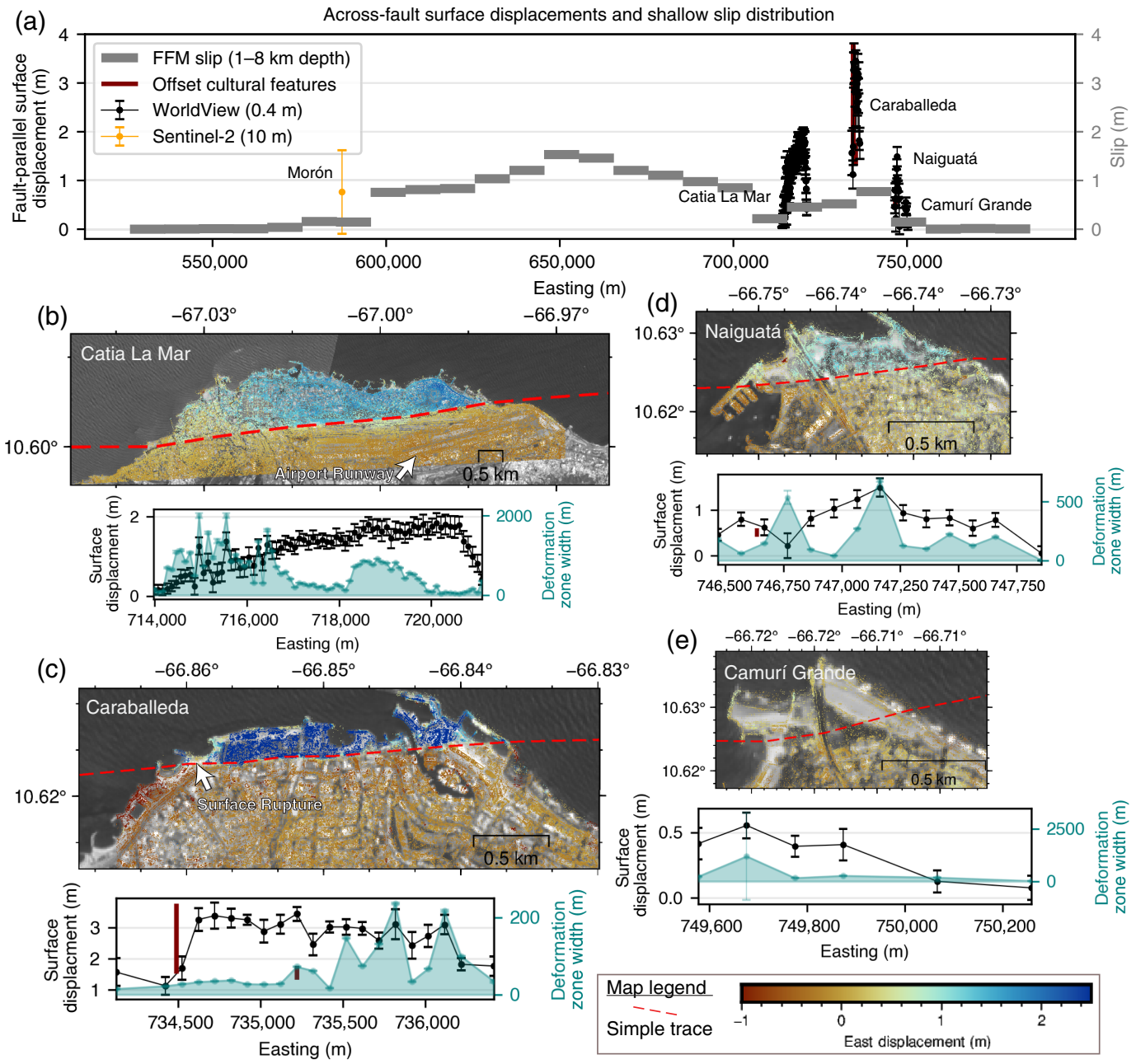
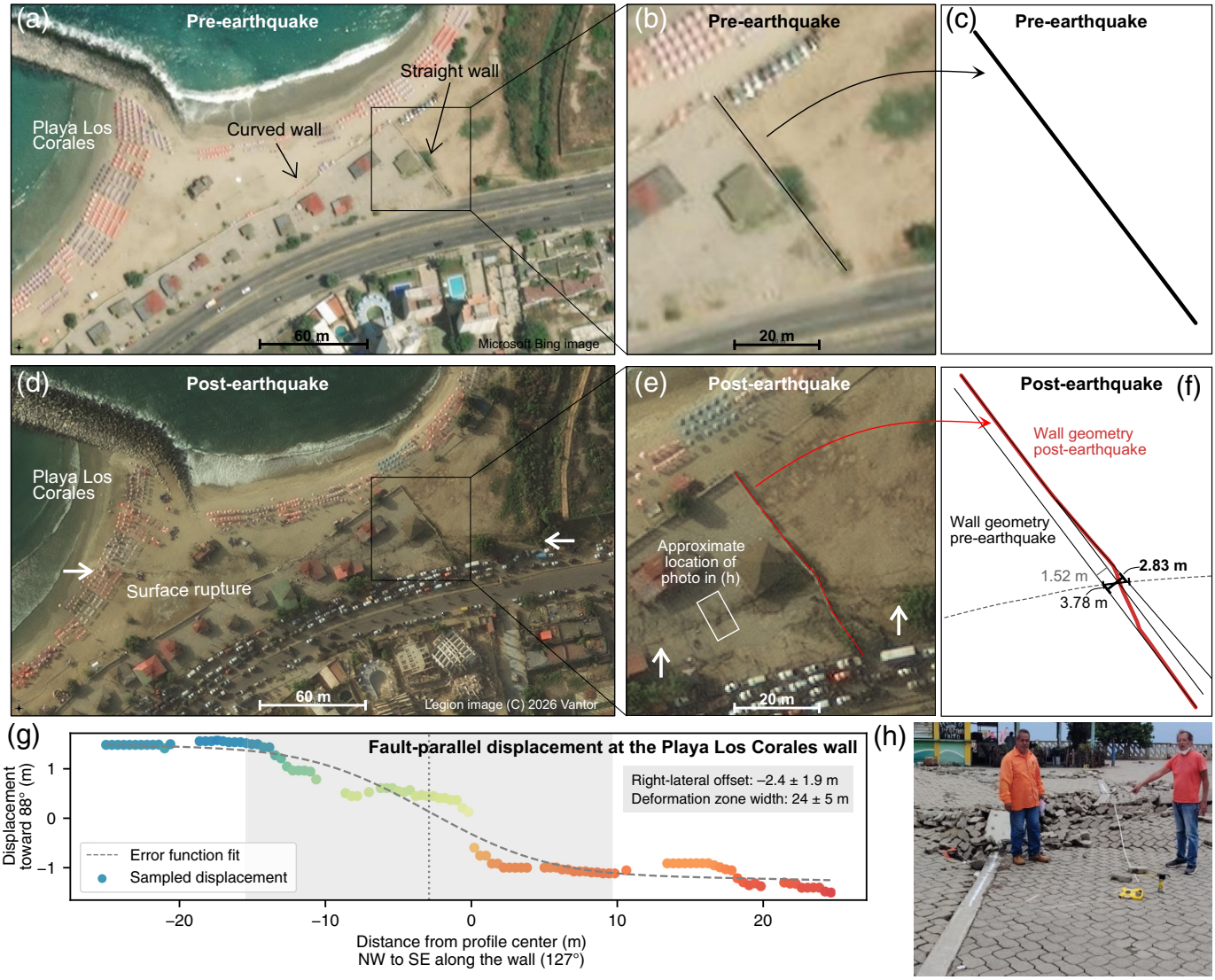


Figure 2. Surface offsets, shallow slip, and distributed deformation for the M_w 7.2 and 7.5 earthquakes. (a) The grey bars show the USGS finite-fault model (FFM) slip for rectangular patches from ~1 to 8 km depth (see Data and Resources). Fault-parallel displacements and associated 1-standard deviation uncertainties (black dots and error bars) are derived from error function fits to Sentinel-2 (10 m resolution) optical image subpixel correlation results near Morón and from WorldView (~0.4 m resolution) optical image subpixel correlation results at each of the coastal towns. (b–e) 0.4 m resolution east–west displacement maps for each point (east positive, color bar on bottom right) overlain on Sentinel-2 optical imagery, with scatter plots of offsets (black) measured across the simple fault trace (red dashed line). Deformation zone widths (blue) are plotted on a secondary *y* axis, also measured from the error function fit. Maroon vertical bars bound the range of offsets measured from cultural features in WorldView imagery. The white arrows mark (b) the location of the Simón Bolívar International Airport near Catia La Mar and (c) the location of surface rupture on Caraballeda with 2.1 m of offset measured in the field. Spatial extents of b–e are shown in Figure 1. Figure S1 shows example profiles and the map location of each profile measurement (Hanagan, Reitman, *et al.*, 2026).

Downloaded from pubs.geoscienceworld.org/ssa/tsr/article-pdf/6/4/400/8403143/tsr-2026037.1.pdf by guest on 21 October 2026



should be considered a minimum estimate because the subpixel correlation and error function fitting may smooth over local offsets (e.g., Fig. 3, Fig. S1).

Results

The subpixel correlation results highlight widely distributed deformation on land near Morón, closer to the M 7.2 epicentral region, and narrower deformation farther east at the other coastal towns (Fig. 2). Note that at Camurí Grande, displacements approach the detection limits of the method due to challenging urban, tree, and cloud-covered conditions (at best, one-tenth to suprapixel size uncertainty; Hanagan, DeLong, and Reitman, 2026).

Near Morón, 0.8 ± 0.9 m of fault-parallel displacement along the coast is distributed over a ~3300 m width (Fig. S1 of

Figure 3. Surface rupture at Playa Los Corales, Caraballeda (location marked by white arrow in Fig. 2c). Analysis of (a–c) pre- and (d–f) post-earthquake WorldView optical images reveals <300 m of surface rupture that right laterally offsets a wall (c,f) sub-perpendicular to the local fault strike by ~2.8 m (1.5–3.8 m), in good agreement with subpixel correlation results at this location. (d,e) Surface rupture is visible in the postearthquake image marked by white arrows. The postearthquake WorldView image from 26 June 2026 is available through the Vantor Open Data program. Approximate location of the reported field offset measurement (~2.1 m) is denoted in (e). (g) Fault-parallel displacement from subpixel correlation near the offset wall shown in d–f. (h) Field offset of low concrete structure accommodating a minimum of ~2.1 m right-lateral slip at the location indicated in (e). Professor Ilich Garcia is pictured to the left of Professor Omar Pérez, both from the Department of Earth Sciences, Simón Bolívar University (permission for photo use granted by Professors Garcia and Pérez). NW, northwest; SE, southeast.

Downloaded from pubs.geoscienceworld.org/ssa/tsr/article-pdf/6/4/400/8403143/tsr-2026037.1.pdf by guest on 21 October 2026

Hanagan, Reitman, *et al.*, 2026). The large standard deviation is consistent with the expected noise level from Sentinel-2 subpixel correlation, but the offset is consistent with line-of-sight observations from Sentinel-1 InSAR and preliminary shallow fault-slip estimates (Fig. 2; Hanagan, Reitman, *et al.*, 2026; see Data and Resources for the USGS finite-fault model slip). Note that the finite-fault model is preliminary, relying heavily on teleseismic observations, with a low-resolution patch size (~8 by 10 km) that prevents a direct comparison with surface slip magnitudes. It is useful, however, for broad comparison in the absence of other information for slip at depth. Such low magnitudes of widely distributed displacement are supported by the lack of surface rupture or cracking observed in the 0.3–1.0 m resolution satellite optical imagery.

East of Morón along the coastal towns, the zone of deformation becomes narrower. Right-lateral surface displacement increases eastward on land over Catia La Mar to a maximum of 1.8 ± 0.2 m and a mean of 1.2 ± 0.2 m (Fig. 2). The profiles have no data offshore over the coastal towns, so lower apparent displacements may result from a failure to capture distributed deformation. The average deformation zone width across Catia La Mar is 580 ± 2 m, significantly narrowing eastward toward the airport (Fig. 2). Across-fault displacement attains a maximum at Caraballeda, peaking at 3.5 ± 0.2 m with an average of 2.7 ± 0.3 m. Deformation zone widths average 69 ± 1 m. From Naiguatá to Camurí Grande, displacement decreases. At Naiguatá, the maximum and average displacements are 1.5 ± 0.2 m and 0.8 ± 0.2 m, across an average deformation zone width of 200 ± 7 m. At Camurí Grande, the maximum and average displacements are 0.6 ± 0.1 m and 0.3 ± 0.1 m, distributed over an average 340 m width with equal uncertainty (Fig. 2).

Only minor or discontinuous surface fractures are identified at the scale of the imagery (~0.4 m resolution). The only visible continuous stretch of surface rupture appears along the western coast of Caraballeda on the Playa Los Corales (Fig. 3). Here, <300 m long surface rupture right-laterally offsets a wall by 2.8 m (1.5–3.8 m; Fig. 3). ~20 m to the southwest, the subpixel correlation results show a 2.4 ± 2 m offset, not coinciding with the exact location of the wall because the results decorrelate. A nearby field measurement records 2.1 m of offset over a distance of ~2 to 3 m along a narrow concrete line, likely representing a minimum offset value because the exact fault-parallel direction and magnitude of distributed deformation are difficult to capture in the field (Fig. 3). Offsets were measured manually from cultural features in WorldView imagery at two other locations: from offset crosswalk markings on Caraballeda (1.3–1.8 m), and from initially straight lines in concrete on Naiguatá (~0.5 m; maroon bars in Fig. 2). No discrete rupture was traceable through these features in the imagery.

At the Simón Bolívar International Airport near Catia La Mar, the subpixel correlation results show a primary rupture zone with ~1.2 m of fault-parallel displacement over a width of 50 m, and a secondary zone of rupture ~350 m to the south with ~0.1 to 0.2 m of narrow fault-parallel displacement between June 25 and 26 (Fig. 4). The secondary zone is colocated with cracks that appeared in the runway on June 26 (Fig. 4). The same cracks are not present on June 25, ~23 hr and 50 min earlier. Displacement along the secondary rupture zone is also observed in the correlation results spanning the co- and postseismic timeframe to June 25 (Fig. 4). Notably, the coseismic-inclusive correlation results show increased displacement with distance from the secondary rupture, while the postseismic-only displacements decrease with distance from the secondary zone, although the results are noisy and asymmetric (Fig. 4e, bottom panel).

Discussion

The relative lack of throughgoing surface rupture from the 2026 M_w 7.2 and 7.5 Venezuela earthquakes along the Boconó and San Sebastián faults near Morón, Catia La Mar, Caraballeda, Naiguatá, and Camurí Grande initially raised concern for the presence of a shallow slip deficit that could drive future earthquakes or afterslip. Analysis of high-resolution satellite optical imagery provides critical first-order observations of onshore rupture with mostly distributed surface expression. Nearer to the M_w 7.2 epicentral region by Morón, broad deformation may indicate residual elastic strain (Fig. 1). In contrast, observed deformation gradients at the eastern coastal towns indicate shallow fault slip close to or exceeding slip estimates at depth (Fig. 2). These steep gradients without surface rupture imply shallow deformation processes operating beyond linear elastic constitutive behavior. We propose a generalized elastoplastic framework to describe the range of deformation styles observed onshore along the earthquake rupture (Fig. 5).

Inelastic distributed deformation near the Earth's surface is well described by frictional elastoplastic constitutive laws (e.g., Drucker–Prager, Mohr–Coulomb), where a material deforms elastically until a pressure-dependent yield criterion is reached, after which permanent, plastic strain accrues (e.g., Kaneko and Fialko, 2011; Nevitt *et al.*, 2020). A material's elastic strain limit depends on both the elastic moduli and the yield parameters. Poorly consolidated surface material, such as coastal alluvium, may be likely to host large strains through permanently

Downloaded from pubs.geoscienceworld.org/ssa/tsr/article-pdf/6/4/400/8403143/tsr-2026037.1.pdf by guest on 21 October 2026

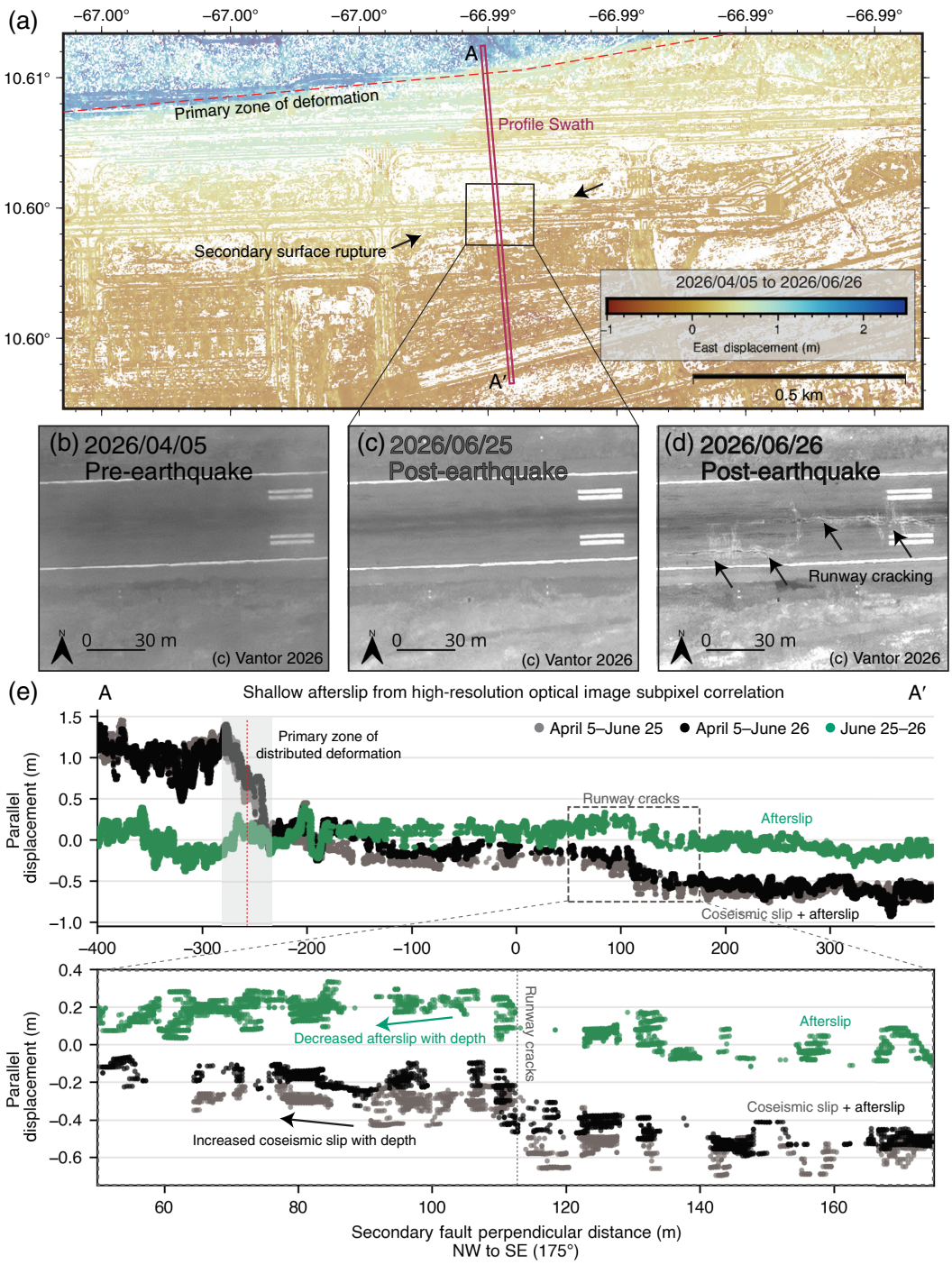
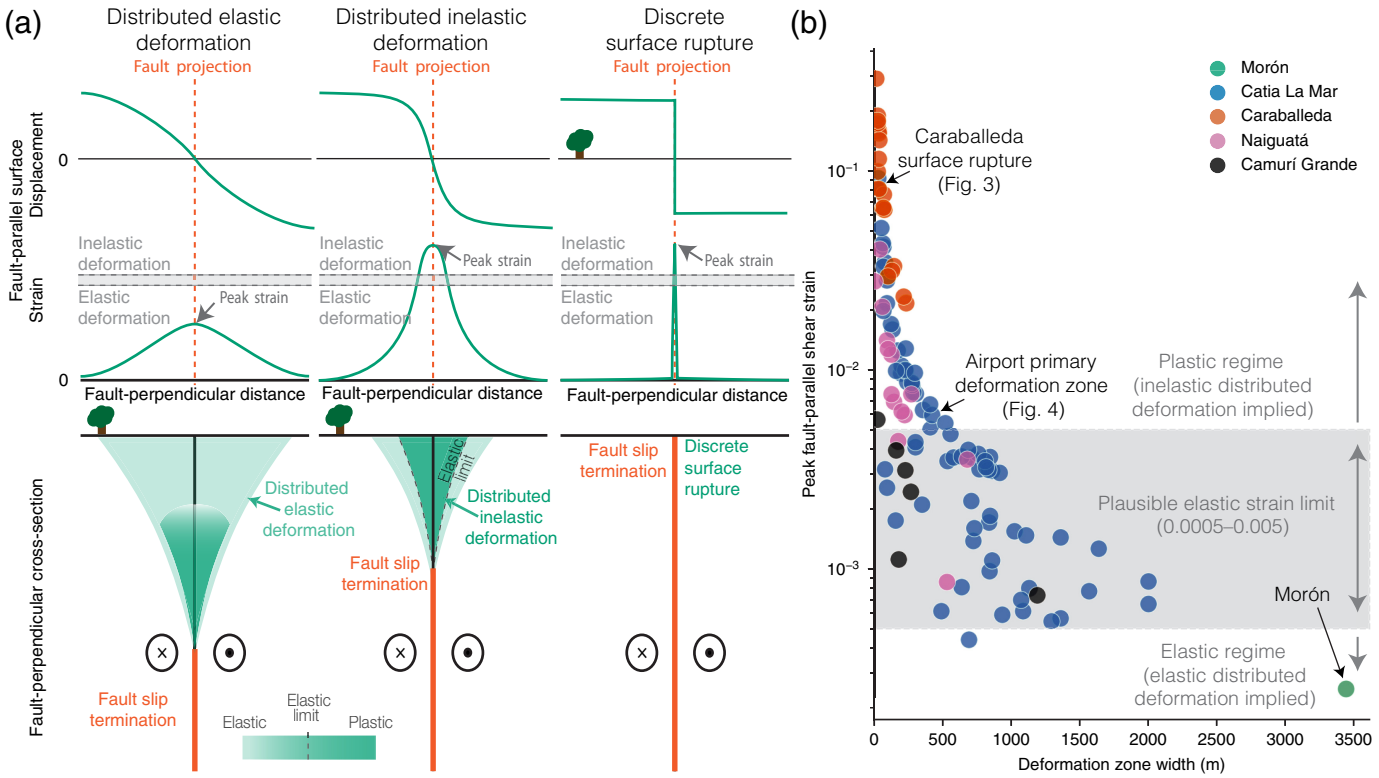


Figure 4. Observations of distributed deformation and afterslip from optical imagery at the Simón Bolívar International Airport. (a) Map of east–west (east positive) displacements spanning the coseismic to two-day postseismic timeframe (26 June) from subpixel correlation of WorldView images. A secondary fault trace is inferred from the displacements ~350 m south of the simple fault trace (red dashed) in (b–d), the black box. Visible cracks formed in this area on the tarmac between WorldView images collected on (c) 25 June and (d) 26 June, respectively. (e) Fault-parallel displacements (positive toward 85°) from a 10 by 800 m swath across the primary zone of distributed deformation and secondary fault trace shown in (a). The combined coseismic and postseismic displacements to 25 and 26 June are shown as gray and black scatter points, respectively, and the isolated postseismic displacement from 25 to 26 June is shown in green. A ~0.1 to 0.2 m offset is visible at the location of the cracked tarmac, and little deformation with distance from the cracks. The comparison of the combined coseismic and afterslip-only results reveals potential shallow propagation of slip in the uppermost tens of meters.

Downloaded from pubs.geoscienceworld.org/ssa/tsr/article-pdf/6/4/400/8403143/tsr-2026037.1.pdf by guest on 21 October 2026



distributed deformation without discrete surface rupture (e.g., Kaneko and Fialko, 2011). Detailed characterization of the shallow subsurface material properties from Morón to Camurí Grande is not feasible for this study; instead, we consider a plausible range of elastic limits from 0.0005 to 0.005 (0.05%–0.5%; Lockner, 1998; Nevitt *et al.*, 2020). The upper limit is commonly cited for earthquake studies derived from laboratory tests on confined Westerly Granite (Lockner, 1998; Brooks *et al.*, 2017). The lower bound is decreased by an order of magnitude, consistent with constitutive properties and confining pressures in shallow alluvium (10s m depth; e.g., Nevitt *et al.*, 2020). This range (0.0005–0.005) is intended to bracket reasonable material response rather than represent a measured property, though it may be even lower (Bozzano *et al.*, 2008).

Measured peak shear strains within this simplified elastoplastic framework imply a variety of surface displacement behaviors, including discrete surface rupture with strains above the elastic limit, and/or fully distributed deformation with strains spanning below and above the plausible elastic strain limit (Fig. 5). Correspondingly, low-magnitude, widely distributed displacement is more consistent with predominantly elastic deformation at Earth's surface while strains exceeding the plausible elastic limit range suggest permanent, inelastic deformation at Earth's surface.

Figure 5. Simplified framework with strain from discrete surface rupture and distributed elastic and inelastic surface deformation considering an elastoplastic constitutive model with a frictional fault. (a) Schematic of three modes of displacement and strain above a strike-slip fault with slip that terminates deep, shallow, or at the surface. The endmember examples demonstrate where peak strain remains below or exceeds the plausible elastic strain limit, labeled as discrete surface rupture along a frictional fault or distributed deformation dominantly in the elastic or plastic regimes. Distributed displacement in the elastic regime is recoverable, and distributed displacement above the elastic strain limit is permanent. (b) Peak static fault-parallel shear strain versus the 2-standard-deviation deformation zone width from the subpixel correlation error function fits (see measurements of Fig. 3), which likely represent minimum strain and maximum fault zone width estimates. A plausible range of elastic strain limits (gray shading) is shown to distinguish primary shallow plastic and elastic distributed deformation. Examples of (1) discrete surface rupture at Playa Los Corales on Caraballeda, (2) inelastic, permanent distributed deformation at the Simón Bolívar International Airport, and (3) elastic, recoverable distributed deformation near Morón are labeled for comparison.

Surface displacement near the coast by Morón exhibits the lowest strain magnitude, expected to unambiguously fall in the elastic deformation regime even if the full deformation zone is in weak, loosely consolidated alluvium (Fig. 5). The largest slip magnitudes (>1 m) are deeper than 10 km from the preliminary USGS finite-fault model (see Data and Resources). Because no

Downloaded from pubs.geoscienceworld.org/ssa/tsr/article-pdf/6/4/400/8403143/tsr-2026037.1.pdf by guest on 21 October 2026

major earthquakes have occurred on the Boconó and San Sebastián faults in this region since the magnitude 7.1 and 7.4 1812 events (Choy *et al.*, 2010; Fig. 1), we might expect significant shallow interseismic elastic strain accrual that has not eroded any existing shallow slip deficit. Likewise, the faults have no documented shallow interseismic creep to alleviate an inferred potential slip deficit (e.g., Pérez *et al.*, 2001). Therefore, this portion of the rupture is most likely to host a shallow slip deficit with residual elastic strain relative to deeper slip inferred for the 2026 earthquakes, with potential for future seismic or aseismic slip in the uppermost couple of kilometers of the subsurface (Fig. 2; Marone *et al.*, 1991). Future monitoring efforts and a detailed comparison of historic fault-slip estimates with paleoseismic fault-slip rates may reveal whether shallow afterslip will close the slip deficit, or if some other interseismic process in the bulk shallow crust might also accommodate permanent distributed deformation (e.g., Fialko *et al.*, 2005; Baden *et al.*, 2022).

The peak fault-parallel shear strains imply significant permanent deformation at the surface farther east, with slip shallowly buried at 10s–100s m depth. Along the onshore rupture, both fault-parallel surface slip and peak strains tend to increase toward the location of highest inferred shallow displacement from the finite-fault model on Caraballeda, and taper toward the western and easternmost extents of Catia La Mar and Camurí Grande (Figs. 2 and 5). Across Catia La Mar, a clear increase in strain from potentially below to exceeding the elastic limit may suggest shallowing of slip eastward along the 8 km stretch of the fault, resulting in a transition from elastic to primarily permanent distributed deformation (Fig. 5). Almost all near-fault strains at Caraballeda exceed the elastic strain limit. The observation of surface rupture at Playa Los Corales is clear inelastic failure (Figs. 3 and 5). The lack of obvious surface rupture elsewhere on Caraballeda, despite the highest measured near-surface fault-parallel displacement of ∼3.4 m (Fig. 2), likely indicates distributed inelastic deformation in coastal alluvium. The corresponding narrow deformation zone widths (<70 m) indicate shallow slip terminating within 10 s of meters of the surface, with the caveat that the extensive built environment may also alter the surface rupture expression. Similarly, deformation at Naiguatá falls in the regime of permanent inelastic deformation with high strains (Fig. 5). In contrast, strain magnitudes over Camurí Grande are intermediate (Fig. 5), and require better constraints on the mechanical properties and/or field investigations to confirm evidence of plastic yielding. The eastern taper in displacement over Camurí Grande coincides with the inferred end of rupture for the 1900 M_w 7.7 earthquake (Colón *et al.*, 2019), where prestress on the fault may have been lower, favoring less slip during the 2026 M_w 7.5 earthquake.

A closer look at near-surface displacements subparallel to the Simón Bolívar International Airport runway exemplifies a spectrum of deformation processes, with distributed coseismic deformation surrounding the primary rupture and a shallow slip deficit that promotes afterslip on a secondary strand (Fig. 4). The primary zone of displacement north of the runway has no visible discrete rupture at the resolution of investigated imagery (∼0.4 m) despite strains of >0.04, exceeding the expected elastic limit and implying plastic deformation. ∼350 m to the south, a second zone of localized deformation hosts 0.1–0.2 m of afterslip that coincides with delayed runway cracks. The potential decrease in displacement away from the runway cracks during the postseismic period further supports shallow, meter-scale slip propagation toward the surface from June 25 to 26 (i.e., displacement near the surface catching up to deeper coseismic slip; Fig. 4). The delayed aseismic activation of subparallel fault strands hundreds of meters apart highlights the variable nature of fault slip on neighboring structures. Similar observations of the afterslip on a mainshock subparallel fault strand occurred following the 2019 M_w 7.1 Ridgecrest earthquake (Brooks *et al.*, 2020). The secondary strand may be more prone to velocity-strengthening afterslip or triggered creep, sensitive to dynamic or static stress perturbations (Marone *et al.*, 1991; Du *et al.*, 2003). Together, these observations demonstrate varied spatial scales of distributed elastic and inelastic deformation mechanisms along the San Sebastián fault zone. The primary zone of deformation with high, permanent strain is distributed with no fracturing, capturing only part of the total across-fault displacement. Further displacement is accommodated in the secondary deformation zone with brittle surface fracturing overlying frictional fault afterslip that implies residual elastic strain driving closure of a minor shallow slip deficit.

Conclusions

The devastating 24 June 2026, M_w 7.2 and 7.5 Venezuela earthquakes ruptured eastward along the right-lateral Boconó and San Sebastián faults, remaining offshore for ∼70% of their total length. Only one known location of discrete surface rupture is documented, and how deep slip interacted with the surface is important for characterizing shallow fault displacement processes and hazard. Key findings from analysis of high-resolution (WorldView 0.4 m and Sentinel-2 10 m) satellite optical imagery at the sparse locations where the fault crosses onshore suggest:

Downloaded from pubs.geoscienceworld.org/ssa/tsr/article-pdf/6/4/400/8403143/tsr-2026037.1.pdf by guest on 21 October 2026

- Distributed shallow elastic deformation above deeper slip along the coast near the M_w 7.2 epicentral region signifies a shallow fault-slip deficit that may be recovered as future coseismic rupture or afterslip.
- Distributed inelastic, permanent deformation along each of the coastal towns where the fault crosses alluvial fans onshore, with shallowly buried slip in the uppermost tens to hundreds of meters.
- A single continuous, <300 m long stretch of surface rupture with ~2.8 m right lateral offset on the Playa Los Corales of Caraballeda.
- 0.1–0.2 m of shallow afterslip in a secondary fault zone that coincides with delayed runway cracking at the Simón Bolívar International Airport.

Overall, surface displacement observations from the Venezuela earthquakes demonstrate a spectrum of distributed deformation characteristics, highlighting the importance of understanding the mechanical properties of near-surface materials and their effect on fault displacement hazard.

Data and Resources

The U.S. Geological Survey provides up-to-date information for the M_w 7.2 and 7.5 earthquakes (https://earthquake.usgs.gov/earthquakes/eventpage/us6000t7zc/executive; https://earthquake.usgs.gov/earthquakes/eventpage/us6000t7zc/executive; https://earthquake.usgs.gov/earthquakes/eventpage/us6000t7zp/executive; https://earthquake.usgs.gov/earthquakes/eventpage/us6000t7zp/executive; last accessed July 2026), including origin information, moment tensor modeling, finite-fault model and data, and impact. The supplemental material for this article includes other data, processing information, and derived products, including the extended Methods section, Table S1, Figure S1, displacement maps, fault-parallel displacements, and simple trace and is available from Hanagan, Reitman, *et al.* (2026). All high-resolution images for mapping or correlation are available from the Vantor Open Data Program (2026) and to U.S. Government scientists through the USG+ license.

Declaration of Competing Interests

The authors acknowledge that there are no conflicts of interest recorded.

Acknowledgments

This work was funded by the U.S. Geological Survey Earthquake Hazards Program.

Any use of trade, firm, or product names is for descriptive purposes only and does not imply endorsement by the U.S. Government.

References

Antoine, S. L., Y. Klinger, K. Wang, and R. Bürgmann (2024). Coseismic shallow slip deficit accounted for by diffuse off-fault deformation, *Geophys. Res. Lett.* **51,** e2024GL110798, doi: 10.1029/2024GL11.

Audemard, F. A., M. Machette, J. W. Cox, R. L. Dart, and K. Haller (2000). Map and database of Quaternary faults in Venezuela and its offshore regions, *U.S. Geol. Surv. Open-File Rept. 2000-18*, doi: 10.3133/ofr0018.

Baden, C. W., D. L. Shuster, F. Aron, J. C. Fosdick, R. Bürgmann, and G. E. Hilley (2022). Bridging earthquakes and mountain building in the Santa Cruz Mountains, CA, *Sci. Adv.* **8,** no. 8, eabi6031, doi: 10.1126/sciadv.abi6031.

Bozzano, F., A. Caserta, A. Govoni, F. Marra, and S. Martino (2008), Static and dynamic characterization of alluvial deposits in the Tiber River Valley: New data for assessing potential ground motion in the City of Rome, *J. Geophys. Res.* **113,** no. B1, doi: 10.1029/2006JB004873.

Brooks, B. A., S. E. Minson, C. L. Glennie, J. M. Nevitt, T. Dawson, R. Rubin, T. L. Ericksen, D. Lockner, K. Hudnut, V. Langenheim, *et al.* (2017). Buried shallow fault slip from the South Napa earthquake revealed by near-field geodesy, *Sci. Adv.* **3,** e1700525, doi: 10.1126/sciadv.1700525.

Brooks, B. A., J. Murray, J. Svarc, E. Phillips, R. Turner, M. Murray, T. Ericksen, K. Wang, S. Minson, R. Burgmann, *et al.* (2020). Rapid geodetic observations of spatiotemporally varying postseismic deformation following the Ridgecrest earthquake sequence: The U.S. Geological Survey response, *Seismol. Res. Lett.* **91,** no. 4, 2108–2123, doi: 10.1785/0220200007.

Choy, J. E., C. Palme, C. Guada, M. Morandi, and S. Klarica (2010). Macroseismic interpretation of the 1812 earthquakes in Venezuela using intensity uncertainties and a priori fault-strike information, *Bull. Seismol. Soc. Am.* **100,** no. 1, 241–255, doi: 10.1785/0120080345.

Colón, S., A. Leal, F. Audemard, R. Vásquez, and J. A. Rodríguez (2019). Análisis macrosísmico del sismo Mw~ 7, 6 de San Narciso del 29 de octubre de 1900, aplicando la escala medio-ambiental de intensidad sísmica ESI 2007, Universidad Central de Venezuela, Revista de la Facultad de Ingeniería, Vol. 34, 17 pp.

Du, W.-X., L. R. Sykes, B. E. Shaw, and C. H. Scholz (2003). Triggered aseismic fault slip from nearby earthquakes, static or dynamic effect? *J. Geophys. Res.* **108,** 2131, doi: 10.1029/2002JB002008.

Farr, T. G., P. A. Rosen, E. Caro, R. Crippen, R. Duren, S. Hensley, M. Kobrick, M. Paller, E. Rodriguez, L. Roth, *et al.* (2007). The shuttle radar topography mission, *Rev. Geophys.* **45,** RG2004, doi: 10.1029/2005RG000183.

Fialko, Y., D. Sandwell, M. Simons, and P. Rosen (2005). Three-dimensional deformation caused by the Bam, Iran, earthquake and the origin of shallow slip deficit, *Nature* **435,** 295–299, doi: 10.1038/nature03425.

Downloaded from pubs.geoscienceworld.org/ssa/tsr/article-pdf/6/4/400/8403143/tsr-2026037.1.pdf by guest on 21 October 2026

Hanagan, C., S. B. DeLong, and N. G. Reitman (2026). Effect of land cover type on 3D deformation recovery from synthetically deformed high resolution satellite optical imagery, *Earth Space Sci.* **13,** e2025EA004477, doi: 10.1029/2025EA004477.

Hanagan, C., N. G. Reitman, W. D. Barnhart, and R. Schmitt (2026). Remote observations of surface deformation for the M 7.2 and M 7.5 2026 Venezuela earthquakes (provisional release), *U.S. Geol. Surv. Data Release*, doi: 10.5066/P13QPYJX.

Kaneko, Y., and Y. Fialko (2011). Shallow slip deficit due to large strike-slip earthquakes in dynamic rupture simulations with elasto-plastic off-fault response: Modelling shallow slip deficit, *Geophys. J. Int.* **186,**no. 3, 1389–1403, doi: 10.1111/j.1365-246X.2011.05117.x.

Larsen, M. C., G. F. Wieczoreck, L. S. Eaton, B. A. Morgan, and H. Torres-Sierra (2002). Natural hazards on Alluvial Fans: The Venezuela debris flow and flash flood disaster, *U.S. Geol. Surv. Fact Sheet 103-01*, 4 pp., doi: 10.3133/fs10301 (English and Spanish).

Lockner, D. A. (1998). A generalized law for brittle deformation of Westerly granite, *J. Geophys. Res.* **103,** no. B3, 5107–5123, doi: 10.1029/97JB03211.

Marone, C. J., C. H. Scholtz, and R. Bilham (1991). On the mechanics of earthquake afterslip, *J. Geophys. Res.* **96,** no. B5, 8441–8452, doi: 10.1029/91JB00275.

Martinez, C. (2026). Venezuela earthquakes of 24 June 2026 (M7.2 + M7.5) (Version 1.2) [Dataset], *Zenodo*, doi: 10.5281/zenodo.21346598.

Milliner, C., A. Donnellan, S. Aati, J.-P. Avouac, R. Zinke, J. F. Dolan, K. Wang, and R. Bürgmann (2021). Bookshelf kinematics and the effect of dilatation on fault zone inelastic deformation: Examples from optical image correlation measurements of the 2019 Ridgecrest earthquake sequence, *J. Geophys. Res. Solid Earth* **126,** e2020JB020551, doi: 10.1029/2020JB020551.

Nevitt, J. M., B. A. Brooks, R. D. Catchings, M. R. Goldman, T. L. Ericksen, and C. L. Glennie (2020). Mechanics of near-field deformation during co-and post-seismic shallow fault slip, *Sci. Rep.* **10,** no. 1, 5031, doi: 10.1038/s41598-020-61400-9.

Pérez, O. J., R. Bilham, R. Bendick, J. R. Velandia, N. Hernández, C. Moncayo, M. Hoyer, and M. Kozuch (2001). Velocity field across the southern Caribbean plate boundary and estimates of Caribbean/South-American plate motion using GPS geodesy 1994–2000, *Geophys. Res. Lett.* **28,** no. 15, 2987–2990, doi: 10.1029/2001GL013183.

Rodriguez Padilla, A. M., M. E. Oskin, C. W. D. Milliner, and A. Plesch (2022). Accrual of widespread rock damage from the 2019 Ridgecrest earthquakes, *Nature Geosci.* **15,** no. 3, 222–226, doi: 10.1038/s41561-021-00888-w.

Styron, R., and M. Pagani (2020). The GEM global active faults database, *Earthq. Spectra* **36,** no. 1_suppl, 160–180, doi: 10.1177/8755293020944182.

Thingbaijam, K. K., P. Martin Mai, and K. Goda (2017). New empirical earthquake source-scaling laws, *Bull. Seismol. Soc. Am.* **107,** no. 5, 2225–2246, doi: 10.1785/0120170017.

Vantor Open Data Program (2026). Available at https://vantor.com/company/open-data-program/ (last accessed July 2026).

Weber, J. C., T. H. Dixon, C. DeMets, W. B. Ambeh, P. Jansma, G. Mattioli, J. Saleh, G. Sella, R. Bilham, and O. Pérez (2001). GPS estimate of relative motion between the Caribbean and South American plates, and geologic implications for Trinidad and Venezuela, *Geology* **29,** no. 1, 75–78.

Wells, D., and K. Coppersmith (1994). New empirical relationships among magnitude, rupture length, rupture width, rupture area, and surface displacement, *Bull. Seismol. Soc. Am.* **84,** no. 4, 974–1002, doi: 10.1785/BSSA0840040974.

Manuscript received 28 July 2026
Published online 13 October 2026

Downloaded from pubs.geoscienceworld.org/ssa/tsr/article-pdf/6/4/400/8403143/tsr-2026037.1.pdf by guest on 21 October 2026